Article:
Alfano, FO, Di Renzo, A, Di Maio, FP et al. (1 more author) (2021) Computational analysis of triboelectrification due to aerodynamic powder dispersion. Powder Technology, 382. pp. 491-504. ISSN 0032-5910

https://doi.org/10.1016/j.powtec.2021.01.011

Computational Analysis of Triboelectrification Due to Aerodynamic Powder Dispersion

Francesca Orsola Alfano[a] , Alberto Di Renzo[a,1], Francesco Paolo Di Maio[a], Mojtaba Ghadiri[b]

[a] *DIMES Department, Università della Calabria, Via P. Bucci cubo 42C, 87036 Rende (CS), Italy*

[b] *School of Chemical and Process Engineering, University of Leeds, Leeds LS2 9JT, UK*

Abstract

Triboelectric charging can strongly influence bulk powder flow behaviour, and hence its characterization is of great interest for safe manufacturing operations. In a recent development, the use of an aerodynamic disperser, employing a pressure pulse to disperse a small powder quantity, shows a great potential for inducing triboelectric charge transfer. We analyse this process by coupled Discrete Element Method and Computational Fluid Dynamics (DEM-CFD) simulations, incorporating triboelectric charge transfer. The simulations are based on property data of glass ballotini as model particles, together with those of α-lactose monohydrate (α-LM) and aspirin, as powders of practical interest. The characteristics of particle-particle and particle-wall collisions are analysed in detail. The analysis shows that pharmaceutical particles charge significantly more than glass ballotini. The charge-to-surface area ratio is remarkably constant and close to its equilibrium value for each test material. Overall, the analysis provides a great insight on the triboelectric charging by aerodynamic dispersion.

Keywords

Triboelectric charging; Powder dispersion; Computational modelling; Pharmaceutical powders; Discrete Element Method; MFIX-DEM.

[1] Corresponding author. Tel: +39 0984 496654 , email: alberto.direnzo@unical.it

1. Introduction

Powders and grains may become triboelectrically charged in handling and processing operations, such as pneumatic conveying, milling, mixing and sieving, due to frequent particle collisions and sliding. High charges on particles can give rise to a variety of electrostatic problems: strong adhesion to containing walls and deposition in pipes, impairing flowability and aggravating segregation of components in a mixture when in dispersed form, e.g. in pneumatic conveying and, in extreme cases, dust explosion. Triboelectrification is the origin of such problems and the underlying mechanisms are the topic of numerous investigations in the literature, as reviewed by Matsusaka et al. [1] and Naik et al. [2]. Despite this, basic questions on the nature of the charge carriers or the charge transfer mechanisms are still open [3-7].

The flow of organic particles and powders like granular polymers, pharmaceutical excipients and ingredients, is severely affected by charge build-up during processing, as the particles have high electrical resistivity. This often leads to handling and processing difficulties, such as uneven dosage, loss of valuable materials and manufacturing stoppages due to powder blocking the pipe line. Therefore, the ability to predict, characterize and control the charge accumulation in processes using powders is particularly attractive. The characterisation of triboelectric charging tendency of new active pharmaceutical ingredients (API) is particularly of great interest and at the same time very challenging, as in the early stages of drug development, there is often a very small quantity of material available for testing. For this reason, Zarrebini et al. [8] used the aerodynamic disperser of an automatic imaging instrument for charging the powder, for which the test powder was sandwiched between two exploding metal films for dispersion. Particles sliding contacts with the films and their subsequent collisions with surfaces of the containing walls brought about electric charge transfer. More recently, Zafar et al. [9] have used the dispersion unit of Morphologi G3® (Malvern Panalytical, Worcestershire, UK) for this purpose. The unit is modified for triboelectrification using different materials based on triboelectric series for inducing charge transfer. It is mounted immediately on top of a Faraday cup to measure the triboelectric charge. A pulse of pressurised gas, commonly air, is used to disperse the powder. The design of the internals of the disperser is such that particles collide repeatedly with the internal surfaces through which charge transfer takes place. As the dispersed powder is immediately dispensed into the cup, there is no charge decay. The ability to examine small amounts of materials (of order of few milligrams) is very attractive for high value materials like APIs and specialty chemicals. The same approach has also been used to assess the breakability of high value fragile particles [10, 11].

There is a need to gain a better understanding of the triboelectric charging processes by impact due to aerodynamic dispersion, not only in this device but also for Dry Powder Inhalers [12]. Therefore, Ali and Ghadiri [13] carried out a piece of simulation work using Computational Fluid Dynamics (CFD) with Lagrangian particle tracking and the charge transfer model of Matsusaka et al. [14] and showed that the triboelectrification of powders during dispersion could be simulated and analysed at the single particle level. However, the particle-particle collisions with the corresponding inter-particle charge transfer were neglected. In addition, the Lagrangian tracking technique, which is most suited for dilute conditions due to the fluid-to-particle one-way coupling, may have influenced the quality of the simulated dispersion during the initial stages, in which the powder is transformed for a dense-phase heap to a dispersed phase.

To study systems with high solids concentrations, Euler-Euler simulation techniques have also been used. By implementing an appropriate Eulerian charging model coupled with a two-fluid model, the level of charge accumulated in fluidized beds due to triboelectrification can be predicted with a good reliability [15], even in bi-disperse systems [16].

DEM-CFD has been used extensively to solve the coupled motion of gas and particle under a wide range of packing and flow conditions [17]. The abilities of DEM to track the motion and collisions of individual particles with the walls and other particles and the soft-sphere approach adopted to represent the contact allow the charging process to be captured in detail. Indeed, all charging events, like particle-particle contact and particle-wall collisions, can be dynamically tracked and the transient loading process fully characterized. In the literature, such an approach has been used to model the contact charging during pneumatic conveying [18], in fluidized beds [19-21], in a periodic box [22] and pharmaceutical particle processing [23].

In the present study, numerical simulation is utilised to investigate the two-phase flow and charge transfer in the dispersion unit of Morphologi G3® and charge accumulation on the particles by combining CFD of the dispersing air pulse in such a complex geometry with the simulation of particle aero-dispersion and triboelectric charging by Discrete Element Method.

2. Computational model

Our simulations are based on a modelling approach combining the DEM for the solid phase and a local average CFD approach for the fluid phase. The equations governing the motion of the particles and of the fluid are summarized below.

To track the translational and rotational motions of each individual particle in the system, the following equations are solved:

$$m_i \frac{d\boldsymbol{v}_i}{dt} = \sum_{j=1}^{Nc} \boldsymbol{F}_{c,ij} + \boldsymbol{F}_{el,i} + \boldsymbol{F}_{d,i} + \boldsymbol{F}_{b,i} + \boldsymbol{F}_{g,i} \quad (1)$$

$$I_i \frac{d\boldsymbol{\omega}_i}{dt} = \sum_{j=1}^{Nc} \boldsymbol{T}_{c,ij} \quad (2)$$

where m_i, v_i, I_i and ω_i are the i-th particle mass, velocity, moment of inertia and angular velocity, respectively. The summation of external actions includes contact forces, $\sum_{j=1}^{Nc} \boldsymbol{F}_{c,ij}$, electrostatic forces $\boldsymbol{F}_{el,i}$, the gas drag and pressure gradient forces, $\boldsymbol{F}_{d,i}$ and $\boldsymbol{F}_{b,i}$, respectively, and gravity, $\boldsymbol{F}_{g,i}$. In the rotational direction, the summation is on all torque contributions generated by non-collinear collisions.

The fluid phase flow is solved by a locally averaged approximation of the continuity and Navier-Stokes equations for a transient, Newtonian, compressible fluid. The velocity and pressure fields are obtained by numerically integrating the following set of differential equations:

$$\frac{\partial \varepsilon \rho_f}{\partial t} + \nabla \cdot \left(\varepsilon \rho_f \boldsymbol{u}\right) = 0 \quad (3)$$

$$\frac{D\varepsilon \rho_f \boldsymbol{u}}{Dt} = -\nabla p + \nabla \cdot \boldsymbol{\tau} + \boldsymbol{F}_{fp} + \varepsilon \rho_f \boldsymbol{g} \quad (4)$$

where $\boldsymbol{F}_{fp}$ represents the interphase momentum transfer per unit volume between the particles and the fluid. The full system is closed with the definition of such term, which in our formulation reads:

$$\boldsymbol{F}_{fp} = -\frac{\sum_i^{N_p} (\boldsymbol{F}_{d,i} + \boldsymbol{F}_{b,i})}{\Psi} \quad (5)$$

in which N_p is the number of particles in the volume Ψ.

The governing equations are solved by using a computer program largely based on the open-source Fortran code MFIX-DEM developed by the National Energy Technology Laboratory, DOE, US [24, 25]. The original code has been modified especially in the DEM part, with additions in the contact model, the triboelectric charge transfer model (see below) and the gas-solid interaction terms.

The complex geometry of the dispersion unit required for this study is directly imported from a STL file reproducing the interior walls of the dispersion cap, capsule and duct, as shown in Figure 1. It should be noted that the CAD geometry has been designed in-house by the authors

with the aim of recreating the most important features of G3 disperser as close to the actual disperser geometry. Therefore, there might be slight variations from the actual device.

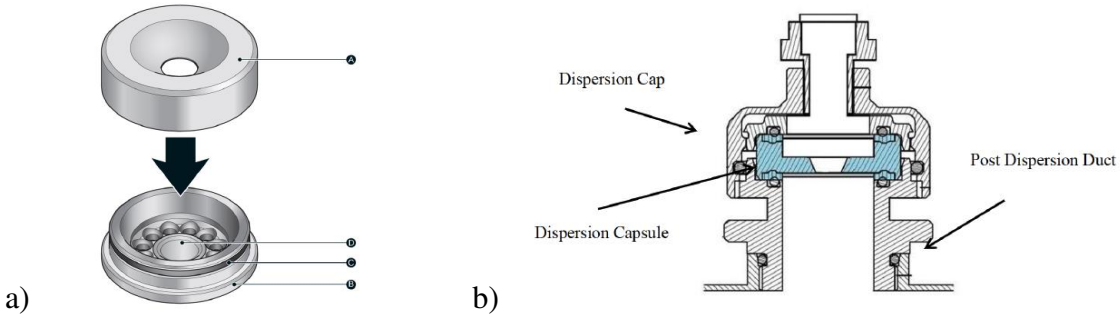

Figure 1. a) Dispersion capsule: (A) Top section, (B) Bottom section, (C) O-ring, (D) Sample well. (Malvern Panalytical Ltd). b) Schematic diagram of the dispersion setup, mounted on top of a Faraday cage for assessing triboelectric charging of particles.

The DEM part of the code uses directly the triangular elements of the CAD file. The domain for the fluid is computed using the Cartesian cut-cell technique available in MFIX-DEM [26], which approximates the fluid volume elements by cutting Cartesian cells whenever they cross a geometric boundary. The architecture of the code allows distributed processing of the calculations, based on MPI. This feature was extensively used in the current work by running the code concurrently on up to 64 cores on a hybrid HPC cluster available at the CheProDeS laboratory – University of Calabria.

2.1 Conventional DEM-CFD

The contact force is computed using the linear spring-dashpot-slider model, whose expressions for the normal and tangential component of the force are (see e.g. [27])

$$F_{c,ij}^{(n)} = -K_n \delta_{n,ij} - \eta_n v_{n,ij} \tag{6}$$

$$F_{c,ij}^{(t)} = min\left(-\mu F_{c,ij}^{(n)}, -K_t \delta_{t,ij} - \eta_t v_{t,ij}\right) \tag{7}$$

where the δ's represent the (normal, sub n, and tangential, sub t) displacements between the contacting particles, v their relative velocity components at the contact point, K the spring stiffness constants, η the dashpot damping coefficients and μ the slider friction coefficient. Note that the tangential contribution of the force is capped in value by Coulomb's sliding limit $\mu F_c^{(n)}$, the rest of the associated energy being dissipated as friction.

Syamlal and O'Brian formula [28, 29] is used for the drag force, which reads:

$$F_d = K_{gs}\left(\vec{u}_s - \vec{u}_g\right) \tag{8}$$

$$K_{gs} = \frac{3}{4}\frac{(1-\varepsilon)\varepsilon\rho_g}{v_{r,s}^2 d_p} C_d\left(\frac{Re_s}{v_{r,s}}\right)\left|\vec{u}_s - \vec{u}_g\right| \tag{9}$$

for which details and definitions are available in the MFIX-DEM documentation guide [24]. The pressure gradient, or generalized buoyancy, force is

$$F_b = -V_p \nabla p \tag{10}$$

where V_p is the particle volume and ∇p is the gradient of the averaged pressure. Other hydrodynamic force contributions are neglected.

2.2 Triboelectric charging model

Depending on the material properties, the charge transfer due to collisions can be either uniform or localized. Models to take account of charge non-uniformity over the surface have been recently proposed [30]. However, in the present work we assume the charge to be a scalar quantity associated with each particle and our triboelectric charging approach is based on the condenser model developed by Matsusaka et al. [14, 31], in the formulation for DEM implementation proposed by Pei et al. [32-34]. The charge transferred from a particle to the wall during each impact, Δq, is calculated as follows:

$$\Delta q = kS_m \Delta V \tag{11}$$

where S_m is the maximum contact area during the impact, ΔV is the potential difference between the two contacting surfaces and k is a charging coefficient. The potential difference term takes into account the contact potential difference and image effects:

$$\Delta V = V_c - V_e = \frac{\Phi_i - \Phi_s}{e} + \xi\frac{q_i z_s}{4\pi\varepsilon_0 R_i^2} \tag{12}$$

Φ_i and Φ_s are the work functions of the particle and the wall surface, respectively; e is the elementary charge; R_i is the particle radius; z_s is the cut-off distance for particle-wall charge transfer (considered as 130 nm); q_i is the charge on the particle before impact; ξ is the image correction factor [35] and is set to 2; ε_0 is the vacuum permittivity (8.854 pF/m).

Substituting Eq. 12 into Eq. 11, the charge exchange during a single particle-wall impact is expressed by:

$$\Delta q = kS_m\left(\frac{\Phi_i - \Phi_s}{e} + \xi\frac{z_s}{4\pi\varepsilon_0}\frac{q_i}{R_i^2}\right) \tag{13}$$

An analogous formula is used to consider the charge transfer from particle i to particle j in a particle-particle contact:

$$\Delta q = kS_m\left(\frac{\Phi_i-\Phi_j}{e}+\frac{z_p}{4\pi\varepsilon_0}\left(\frac{q_i}{R_j^2}-\frac{q_j}{R_i^2}\right)\right) \quad (14)$$

where z_p is the cut-off distance for particle-particle charge transfer and is set to 260 nm [32].

Equations 13 and 14 are used every time a contact is detected in the DEM routine; after each contact, the charge of the particles involved is updated according to:

$$q_{i,new} = q_{i,old} - \Delta q \quad (15)$$

$$q_{j,new} = q_{j,old} + \Delta q \quad (16)$$

Charge accumulated on the particles leads to electrostatic interaction force, according to Coulomb's law. The force acting on particle i due to the interaction with particle j is given by:

$$\vec{F}_{i,j}^{e} = -\frac{1}{4\pi\varepsilon_0}\frac{q_i q_j}{r_{i,j}^2}\hat{n}_{i,j} \quad (17)$$

$\hat{n}_{i,j}$ is the unit vector along the direction connecting the two particles (from i to j) and $r_{i,j}$ is the distance between the centres of the particles. Coulombic interactions between charged particles and the conductive walls of the capsule have also been included in the calculation, according to:

$$\vec{F}_{i,s}^{e} = \frac{1}{4\pi\varepsilon_0}\frac{q_i^2}{(2r_{i,s})^2}\hat{n}_{i,s} \quad (18)$$

in which $r_{i,s}$ is the perpendicular distance between the wall surface and the centre of the particle and $\hat{n}_{i,s}$ is the unit vector from the particle centre and perpendicular to the surface. Eq. 18 is based on the method of image charges (also known as the method of mirror charges) [36]; $\vec{F}_{i,s}^{e}$ is always attractive, since it is due to the interaction between the particle and its mirror image.

The superposition principle is assumed to be valid and the total electrostatic force acting on the i^{th} particle is given by:

$$\vec{F}_{el,i} = \sum_{j=1}^{N}\vec{F}_{i,j}^{e} + \sum_{s=1}^{N}\vec{F}_{i,s}^{e} \quad (19)$$

Electrostatic interactions are evaluated for all the particles whose distance between the centres is smaller than or equal to twice the sum of the radii of the two bodies involved. Such a short range cut-off of electrostatic interaction is adoptable for the present dilute case. The above charging contact model has been coded into the structure of MFIX-DEM. For each detected

contact (both particle-wall and particle-particle), the overlap is recorded, the exchanged charge Δq is calculated and charge values for particles are updated at the end of each collision.

3. Critical model parameters

3.1 Contact stiffness

As already mentioned in section 2, the Linear-Spring-Dashpot model (LSD) has been used for modelling the contact forces in DEM. Despite its simplicity, the LSD model guarantees reliable results, which represent experimental data well [27, 37]. However, one of the main drawbacks of the LSD model is the choice of the contact parameters, such as the normal spring stiffness (K_n) since a procedure to estimate its optimal value is not available [37]. In this particular case, the choice of an appropriate value for the spring stiffness is particularly important, since the exchanged charge is proportional to the maximum contact area, which is strictly correlated to K_n. The best criterion for the choice of the parameter values is to calculate them from the actual mechanical properties of the system. In this work, K_n is calculated by imposing the same maximum contact area during a particle-wall collision for the LSD model as it would be using the Hertz contact model with real material properties, like Young's modulus and Poisson's ratio. This criterion ensures the choice of an appropriate value and guarantees an accurate computation both in the determination of realistic contact deformation and forces and the exchanged charge.

According to Hertz theory [38], the maximum contact area depends directly on the maximum normal displacement δ_n (i.e. normal overlap in simulation). The maximum contact area recorded during a collision (S_m) for the linear model and the Hertz model can be set equal as follows:

$$S_m = \pi R_{eq} \sqrt{\frac{m_{eq}}{K_n}} v_{n,0} = \begin{cases} \pi R_{eq}^2 \left(\frac{15 m_{eq} v_{n,0}^2}{16 E_{eq} R_{eq}^3} \right)^{\frac{2}{5}} & \text{for p} - \text{p contact} \\ \pi R_i^2 \left(\frac{5 \pi \rho v_{n,0}^2}{4 E_{eq}} \right)^{\frac{2}{5}} & \text{for p} - \text{w contact} \end{cases} \tag{20}$$

where the equivalent radius, Young's modulus and mass are given by $R_{eq} = \left(\frac{1}{R_1} + \frac{1}{R_2} \right)^{-1}$, $E_{eq} = \left(\frac{1-\nu_1^2}{E_1} + \frac{1-\nu_2^2}{E_2} \right)^{-1}$ and $m_{eq} = \left(\frac{1}{m_1} + \frac{1}{m_2} \right)^{-1}$. The impact velocity is $v_{n,0}$. The linear contact stiffness can then be obtained for particle-particle and particle-wall collisions:

$$K_n^{PP} = \left[\left(\frac{16}{15}\right)^4 E_{eq}^4 R_{eq}^2 m_{eq} {v_{n,0}}^2\right]^{\frac{1}{5}} \quad (21)$$

$$K_n^{PW} = \frac{16}{15} R \left[\frac{5}{4} \rho \pi E_{eq}^4 v_{n,0}^2\right]^{\frac{1}{5}} \quad (22)$$

3.2 Charge transfer parameters

The condenser model for the charge transfer determines a charge accumulation process that can be simplified to a dynamical process. Equation 13 for the particle-wall collision event can be described in the following terms:

$$\Delta q_i = \frac{1}{n_C}(q_i - q_{eq}) \quad (23)$$

in which two parameters, q_{eq} and $\mathrm{n_C}$ are introduced:

$$q_{eq} = -\frac{4\pi\varepsilon_0 R_i^2}{\xi z_s}\frac{(\Phi_i - \Phi_s)}{e} \quad (24)$$

$$\mathrm{n_C} = \frac{1}{kS_m \frac{\xi z_s}{4\pi\varepsilon_0 R_i^2}} = \frac{1}{k\frac{\xi z_s}{4\varepsilon_0}\left(\frac{5\pi\rho v_{n,0}^2}{4E_{eq}}\right)^{\frac{2}{5}}} \quad (25)$$

For a particle starting neutral, a repeated set of n collisions with the same velocity leads the following model process

$$q_n = \frac{q_{eq}}{n_C}\sum_{i=1}^{n}\left(1 - \frac{1}{n_C}\right)^{i-1} \quad (26)$$

If several collisions occur in succession, one might consider the number of impacts n as a continuous quantity and express Eq. 26 in the following form:

$$q(n) = q_{eq}\left(1 - e^{-\frac{\mathrm{n}}{n_C}}\right) \quad (27)$$

Eq. 27 corresponds to the response of a linear first order dynamical system. In such formula, q_{eq} (eq. 24) is a saturation, equilibrium parameter, i.e. the asymptotic charge acquired after a large number of impacts against the wall. It is directly proportional to the surface area of the spherical particle, $4\pi R_i^2$ (i.e. bigger particles have higher saturation charge values) and depends on the material work functions (Φ). $\mathrm{n_C}$ (eq. 25) is the characteristic number of impacts and represents the rate at which the process reaches charge saturation. It depends on the impact velocity, on the wall and particle's Young's modulus and on the particle density.

The experimental results presented by Matsusaka et al. [14], who studied the electrification of an elastic sphere repeatedly impacting on a metal plate, show that after about 30 collisions a particle has almost reached its saturation charge. This characteristic number of impacts is independent of particle size according to Pei et al. [32]. By imposing that a particle achieves 98% of the equilibrium charge (equivalent to four times the characteristic number of collisions) after 30 collisions, a reasonable estimate for the characteristic number of impacts is $n_C = 30/4 = 7.5$. From Eq. 25, the following formula can be used to estimate the charging coefficient, k:

$$k = \frac{1}{n_C}\left(\frac{4E_{eq}}{5\rho\pi}\right)^{0.4} \cdot v^{-0.8} \cdot \frac{4\varepsilon_0}{\xi z_s} \tag{28}$$

For a glass bead impacting at 10 m/s against a steel plate (see Table 1 for the parameters), this leads to $k = 1.4 \cdot 10^{-3}\,\frac{C}{m^2 V}$. It can be used to evaluate the charge increment per unit surface area after the first impact: $\frac{\Delta q_0}{S_m} = kV_c = 1.4 \cdot 10^{-3}\,\frac{C}{m^2 V} \cdot (5.32 - 5.05)\,V = 3.78 \cdot 10^{-4}\,\frac{C}{m^2}$, in reasonable agreement with the value reported by Watanabe et al. [39], i.e. $\frac{\Delta q_0}{S_m} \approx 10^{-4}\,\frac{C}{m^2}$.

4. Results and discussion

4.1 Model set-up

Spherical shape is used for all simulations, with physical and mechanical properties corresponding to those of glass ballotini, used as model particles and α-lactose monohydrate (α-LM) and aspirin crystals as materials of pharmaceutical relevance. The properties are reported in Table 1. Three particle sizes are used in the simulations for glass ballotini. The physical and mechanical properties of pharmaceutical particles are selected according to Watanabe et al. [39] and Naik et al. [40]. For glass ballotini and stainless steel (AISI 316), the work function values evaluated by Trigwell et al. [41] are used. The work function of aspirin and α-LM are calculated following the same procedure proposed by Gallo and Lama [42] using the software MOPAC2016™ [43, 44]. The chemical structures used for the calculation have been found on online databases[2,3].

[2] http://openmopac.net/PM7_accuracy/data_solids/Aspirin_I__ACSALA01_jmol.html

[3] http://openmopac.net/PM7_accuracy/data_solids/alpha-Lactose_monohydrate__LACTOS10__Jmol.html

Table 1 Mechanical and physical properties of the materials used in the simulations

	Glass ballotini	**A-LM**	**Aspirin**	**AISI 316**
Simulation diameter, D (μm)	109, 78, 53	109	109	-
Density, ρ (kg/m^3)	2500	1525	1400	8000
Young's modulus E (GPa)	70	18	7.2	200[4]
Poisson's ratio, ν	0.22	0.30	0.29	0.27
Friction Coefficient (p-p), μ_{pp}	0.70	0.5	0.5	-
Friction Coefficient (p-w), μ_{pw}	0.52	0.7	0.7	-
Restitution Coefficient (p-p), e_{pp}	0.70	0.4	0.4	-
Restitution Coefficient (p-w), e_{pw}	0.70	0.6	0.6	-
Work function, Φ (eV)	5.32	5.89	6.12	5.05

The calculated values of the contact area for the relevant spring stiffness, assuming an average impact velocity $v = 10$ m/s for particle-particle and particle-wall collisions are given in Table 2.

Four bulk solids volumes, 1, 3, 5 and 7 mm^3 have been simulated based on the experimental work on the same materials, giving rise to the number of particles reported in Table 3.

Table 2 Maximum contact area and stiffness coefficients for 109 μm diameter particles colliding with a stainless-steel wall and between themselves at a relative impact velocity $v = 10$ m/s

	Maximum contact area, S_m (μm^2)		**Spring stiffness, K_n (kN/m)**	
	particle-particle	particle-wall	particle-particle	particle-wall
Glass	60	118	170	360
Aspirin	116	206	25	65
A-LM	83	152	55	135

The shape of the dispersion unit follows that of Morphologi® G3. A batch of particles initially deposited on the sample well, inside the capsule is subjected to an air pressure pulse from the top. Consequently, the particles are spread out radially and then lifted up by encountering a toroidal lip at the perimeter of the well. This causes particle dispersion and multiple collisions with the capsule walls and themselves before passing through a carousel of holes, eventually leaving the domain from the bottom surface. A non-uniform, parallelepipedic structured mesh has been obtained with the Cartesian grid cut-cell technique in MFIX. The grid is denser on the upper part, as a higher resolution is required due to the complex shape of the capsule. The size of the grid has been selected in order to have a good compromise between CFD accuracy and DEM-CFD coupling requirements, which generally set the ratio of the cell size to particle

[4] www.azom.com

diameter to be larger than 2 [45, 46]. The final mesh consists of about 140k cells with an overall average size of about 400 µm; the smallest cells near the holes have an average size of 230 µm.

Dry air at ambient condition ($T = 25°C$, $\mu = 1.827 \cdot 10^{-5}$ Pa·s) is considered under compressible flow conditions. The simulation is three-dimensional and transient. Static air initially at 1 bar and subjected to a sudden inlet pressure change to 1.5 bar is evolved for 20 ms.

In the experimental work, the particles are usually poured into the sample well with a sampling spoon. DEM is used to generate the initial deposition of the particles, letting an initially ordered configuration to settle on the sample well of the capsule for 50 ms. Figure 2 shows such deposition process with the particles coloured by their velocity.

Table 3 Number of spheres used in in the simulation of glass ballotini dispersion

Diameter (µm)	Bulk volume (mm^3)	Number of particles
109	1	343
	3	1728
	5	3456
	7	5376
78	1	1331
	3	5202
	5	7452
	7	13754
53	1	4096
	3	16875
	5	24786
	7	43928

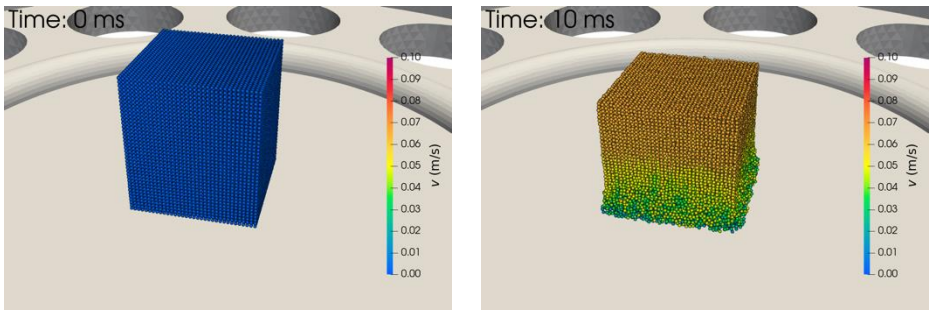

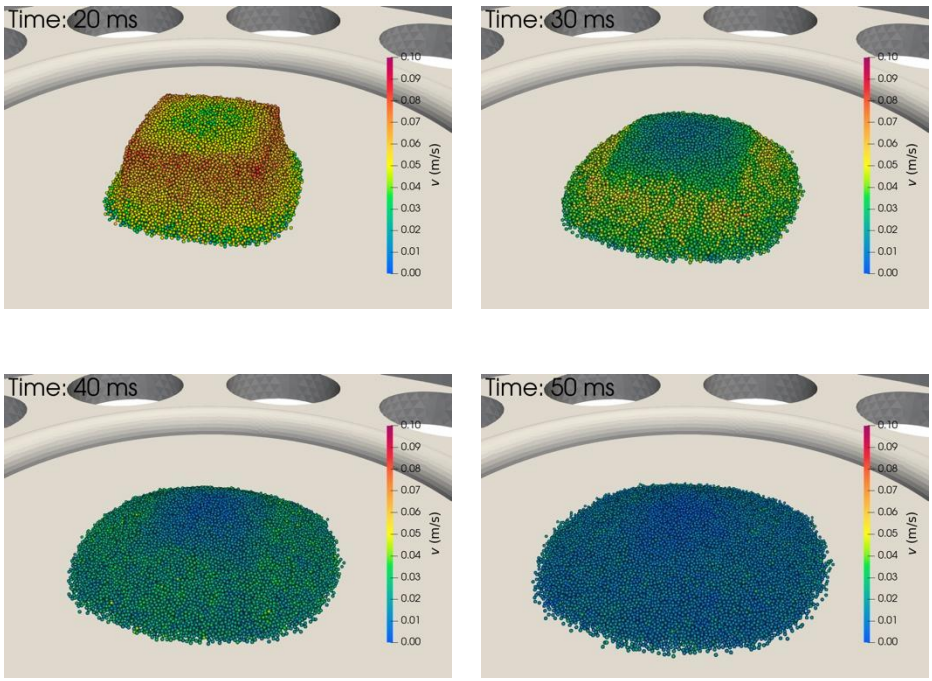

Figure 2. Building of the initial configuration for a 7 mm^3 sample of glass ballotini (53 μm)

4.2 Fluid dynamics of the system

The fluid flow develops from the central region of the top surface (see Figure 1). The air pressure pulse produces a transient axisymmetric impinging jet onto the horizontal surface of the well and then changes direction flowing horizontally and radially outward over the perimeter lip, passing through the thin annular region and eventually through twelve tapered holes on the base, entering the post-dispersion duct. Figure 3 shows the development of the flow field from the very first instant after the start by a colour map of the velocity field along a vertical plane cut along the capsule diameter. The velocity of the gas is shown to increase rapidly and then gradually stabilizes after about 15 ms. Some fluctuations still persist throughout the entire simulation. In the first instant, the velocity field shows very high velocity values (higher than 300 m/s). Very high gas speeds were found also by Ali and Ghadiri [13], who studied the fluid dynamics in a similar device including a Reynolds stress turbulence model; their results show that, if a 3 bar inlet pressure is considered, gas velocities as high as 500 m/s can be reached.

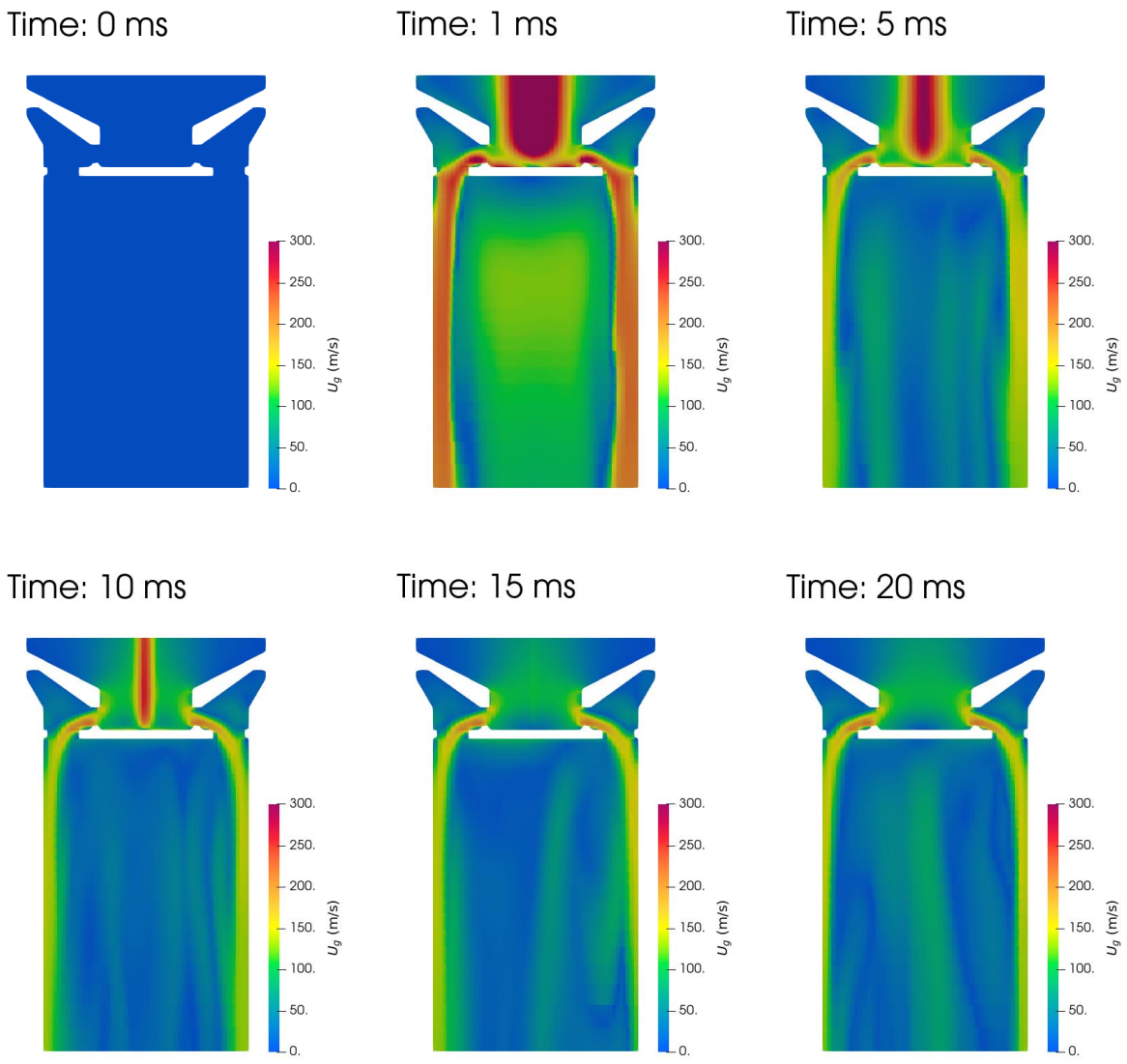

318

319 Figure 3. Colour map of the gas velocity field across a vertical cut plane at different times

320

321 **4.3 Coupled fluid-particle motion**

322 The particle arrangement after settling in the sample well is used as the initial condition for the
323 full DEM-CFD simulations. Zarrebini [47] showed that for contact electrification due to
324 aerodynamic dispersion the initial charge of the sample is negligible and has no influence on
325 the final charge. Thus, the initial charge level is set to zero. Figure 4 shows the top views of the
326 first few instants of a DEM-CFD simulation. The sample with a bulk volume of 5 mm^3 is used
327 here, consisting of 24768 spherical particles with a diameter of 78 μm. The particles are clearly
328 pushed outwards radially by the action of the impinging air jet. They then impact on the toroidal
329 bump around the sample well and jump up and collide with an inclined angle onto the top

surface and reflect back towards the base of the outer annulus. Multiple collisions with the top surface and bottom base take place before the particles eventually go through the holes into the post-dispersion duct before leaving the system from the bottom outlet. DEM results suggest that the toroidal edge is essential for a good dispersion of the sample across the capsule interior as it prevents particles from sliding directly to the holes (see e.g. Figure 4d).

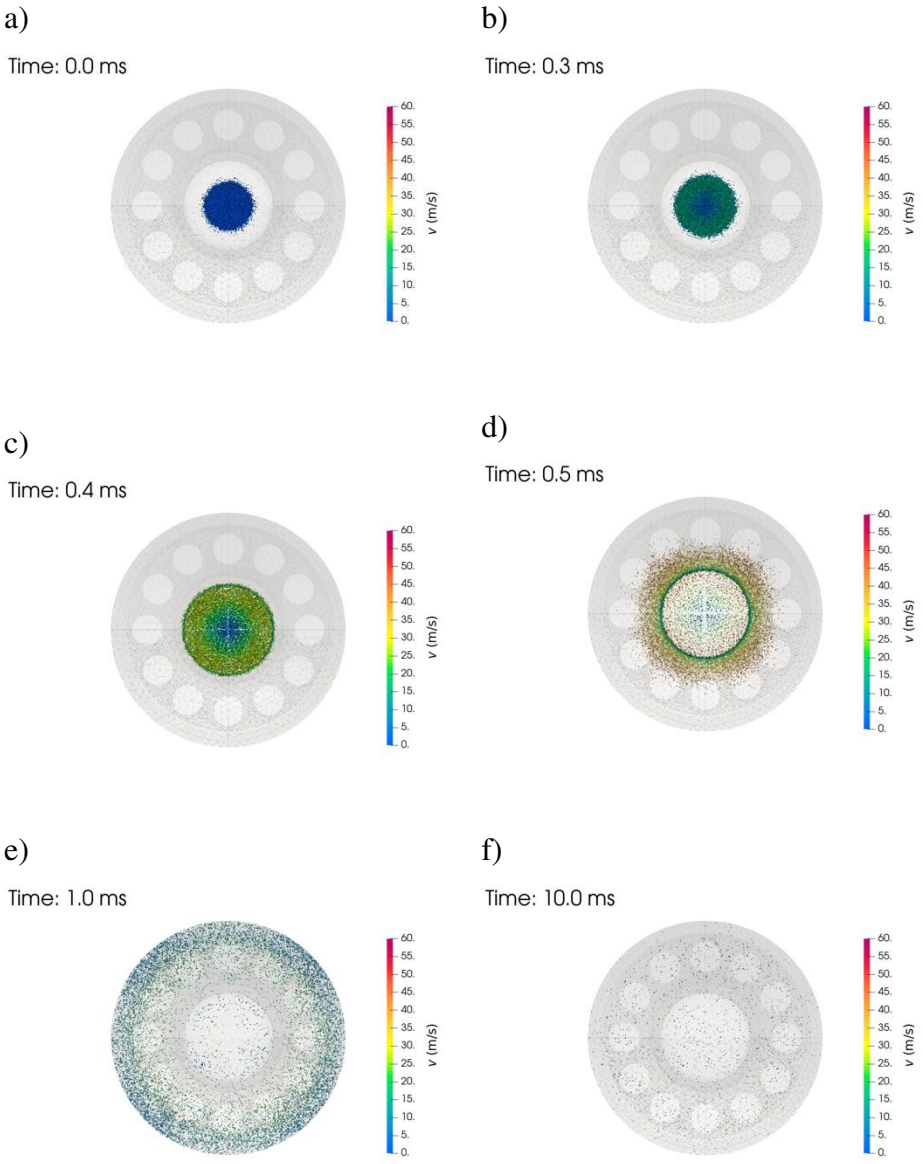

Figure 4. Top view of the simulation results on the motion of the particles inside the capsule device at times 0 ms (a), 0.3 ms (b), 0.4 ms (c), 0.5 ms (d), 1 ms (e), 10 ms (f) from the onset of the air pressure pulse. The sample volume is 7 mm^3 (about 14k particles) of 78 µm diameter spherical particles. Particles are coloured according to their velocity magnitude.

Interparticle and particle-wall collisions are far more frequent at the early stages of dispersion (0.1 – 0.5 ms) than the later stages. Cumulative plots of the total number of collisions divided by the number of particles are shown in Figure 5 for glass particles with different bulk volumes (1 mm^3 and 7 mm^3) for two particle diameters (109 μm and 78 μm). The x-axis is presented in log-scale to highlight the initial changes. Most collisions for both particle-particle and particle-wall occur at the early stages of the dispersion at times shorter than 1 ms, and with all the curves reaching a plateau after about 3 ms. In the two systems with a larger number of particles (5376 and 13754) the average number of inter-particle collisions exceeds by far those of the particle-wall. Indeed, for the 78 μm particle size samples, the average value of interparticle collisions increases by a factor close to 7 switching from the 1 mm^3 sample to the 7 mm^3 one. The larger the number of particles in the sample, the higher is the ratio between particle-particle and particle-wall collisions. The tribo-electric charge transfer, however, starts via particle-wall collisions, as initially all particles have equal (zero) charges and there is no work function difference between particles. As the charge is accumulated on the particle surfaces, interparticle collisions contribute to distributing the charge over the surfaces of all particles.

Figure 6 shows a scatter plot of the impact velocity for all collisions that occur in the simulation with the particle-wall and particle-particle collisions shown separately by red and blue colours. A moving average of the data is also presented to show the trend. High particle impact velocities occur from about 0.4 ms onwards, as high as 60 m/s against the walls and 80 m/s between particles. In all cases considered, the moving average is close to 10 m/s, the value used to estimate the critical model parameters.

a)

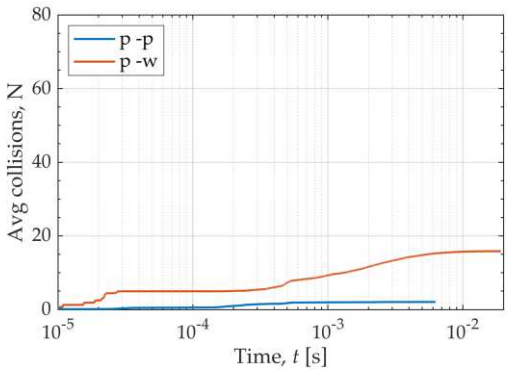

b)

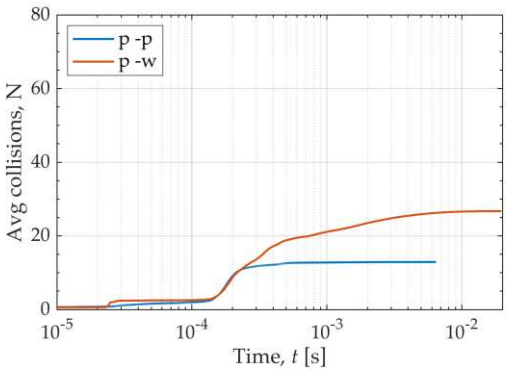

c)

d)

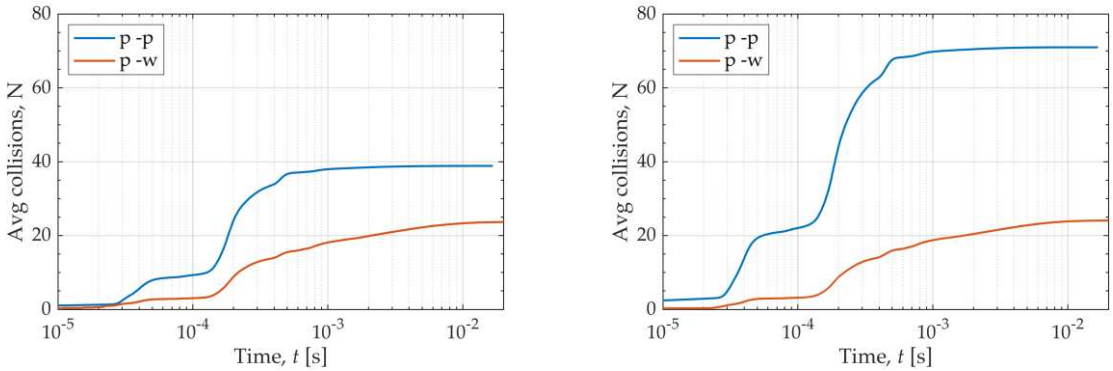

Figure 5. Cumulative number of particle-particle and particle-wall collisions (divided by the number of particles in each simulation) as a function of time for simulations of samples of glass ballotini having different number and size of particles corresponding to indicated bulk volumes: a) 343 (109 µm, 1 mm^3), b) 1331 (78 µm, 1 mm^3), c) 5376 (109 µm, 7 mm^3), d) 13754 (78 µm, 7 mm^3).

a) b)

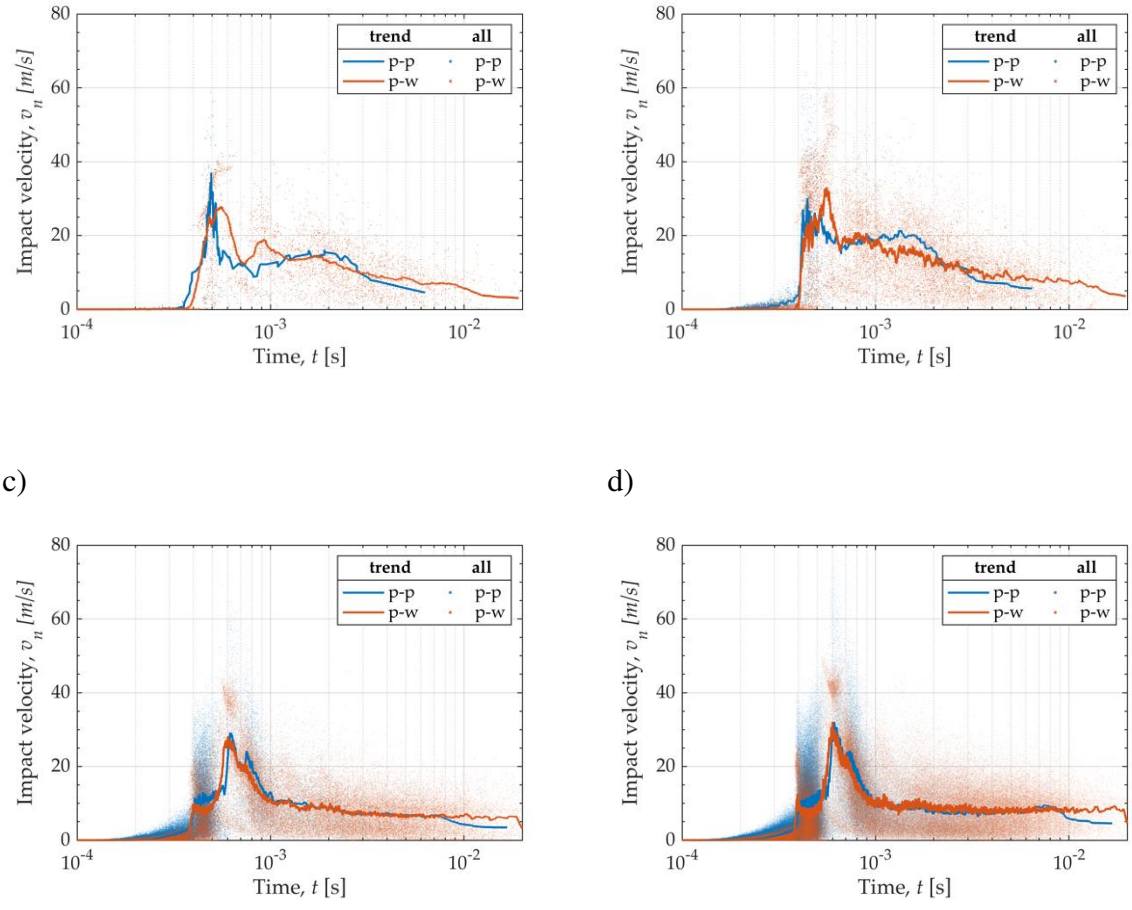

c) d)

Figure 6. Scatter plot of the impact velocity of particle-particle and particle-wall collisions as a function of time for simulations with glass samples having different numbers of particles: a) 343 (109 µm, 1 mm^3), b) 1331 (78 µm, 1 mm^3), c) 5376 (109 µm, 7 mm^3), d) 13754 (78 µm, 7 mm^3). A moving average is also reported for each plot to highlight the trend.

Figure 7 shows the percentage of the initial number of particles inside the system for two simulated cases. The shape of the two curves appears similar: in both cases, after about 12 ms most of the particles have left, as only 5% are still inside for the smaller volume system and 3% in the larger volume one. After 20 ms, which is the pressure pulse duration, the dispersion is complete, with less than 0.1% remaining inside.

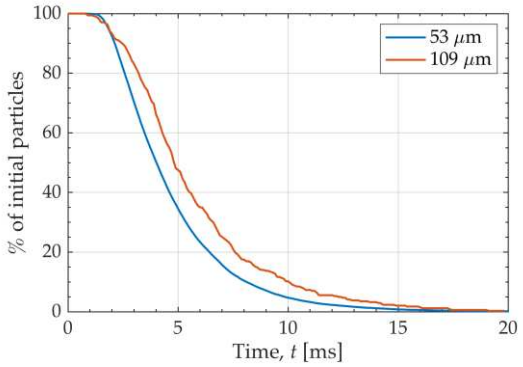

Figure 7 Number percentage of particles remaining in the system as a function of time for glass ballotini simulations for two samples with different amounts and sizes of particles: 343 (109 µm, 1 mm^3), 24786 (53 µm, 5 mm^3)

In Table 4, data on the global characteristics of particle-wall and particle-particle impacts for the two systems considered above are reported. The simulation with the smaller sample volume has a higher average number of impacts, average velocity and maximum velocity.

Table 4. Impact statistics of 78 µm diameter spheres simulating glass particles dispersion.

Particle Number	**1331**	**13754**
Average p-p impacts per particle	13	71
Average p-w impacts per particle	27	24
Max p-p impact velocity (m/s)	74	77
Max p-w impact velocity (m/s)	60	59
Avg p-p impact velocity (m/s)	1.3	1.6
Avg p-w impact velocity (m/s)	5.6	4.7

4.4 Triboelectric charging of glass ballotini

Figure 8 shows the temporal evolution of the total charge acquired by the sample dispersed in the capsule for 1 mm^3 samples of 109 µm and 53 µm glass ballotini. The results are reported in absolute values, but the particles charge negatively against stainless steel. The plots are cumulative: when a particle leaves the device (i.e. reaches the Faraday cage in the experimental system), its last recorded value is stored. After an initial steep increase, the charge gradually reaches a plateau value. The rapid rise is due to particle-wall impacts (see Figure 5). The plateau is gradually reached after approximately 6 ms, when nearly 65% of the particles have already been dispersed outside of the capsule (see Figure 7). The theoretical "equilibrium charge" value is reported for both curves. It is calculated according to Eq. 24 and it is multiplied by the number of particles in the sample. It is noteworthy that the 109 µm sample reaches 79% of its equilibrium charge, while the 53 µm sample gets to 83%.

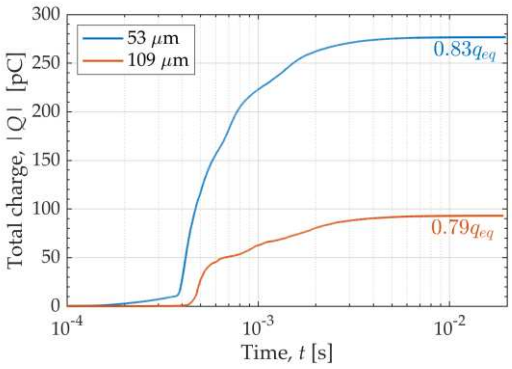

Figure 8 Temporal evolution of the total charge (absolute value) for 1 mm^3 samples of glass particles with two diameters: 109 µm (343 particles), 53 µm (4096 particles). Reference to the theoretical "equilibrium charge" is reported close to the endpoint of each line plot.

Figure 9a shows the absolute charge-to-mass ratio, i.e. the total charge acquired by the sample at the end of the simulation divided by the sample mass, acquired by the glass ballotini. The results are for all particle sizes and sample volumes. The particles charge negatively. The data show a slight reduction of particle charge as the sample volume is increased. The trend is consistent with particle collisions shown in Figure 5(a), where a lower sample mass inside the device promotes particle-wall collisions instead of particle-particle collisions.

More importantly, smaller particles acquire a higher amount of specific charge. This is expected as their specific surface area is larger. Triboelectric charging is essentially a surface phenomenon, so the acquisition of charge per unit mass is inversely proportional to the size of the particles [48]. These trends are in agreement with the work of Zarrebini et al. [8] and Zafar

et al. [9]. Figure 9b shows the total charge acquired in the simulations by all glass ballotini samples (all sample volumes and particle sizes) reported as a function of the total surface area of the particles. The trend appears to be remarkably linear, suggesting that the absolute total charge is directly proportional to the total surface area of the sample and independent of the particle size, as also reported in literature ([8], [47-51]). The charge-to-surface area ratio (σ) is represented by the slope of the regression line in Figure 9b, i.e. 6.85 pC/mm^2. Zarrebini et al. [8] measured a charge density of 0.5 pC/mm^2 for glass ballotini. However, the charging system for the latter was based on exploding foil method and hence slightly different from the method used here. The charge density predicted in this work is in fact remarkably close to the experimental value reported by Zafar et al. [9] for 53-63 µm glass ballotini: 6.33 pC/mm^2, usng the same dispersion system. Surprisingly though, in their experimental work the surface charge density varies with particle size, decreasing down to 3.23 pC/mm^2 for 106-112 µm particles.

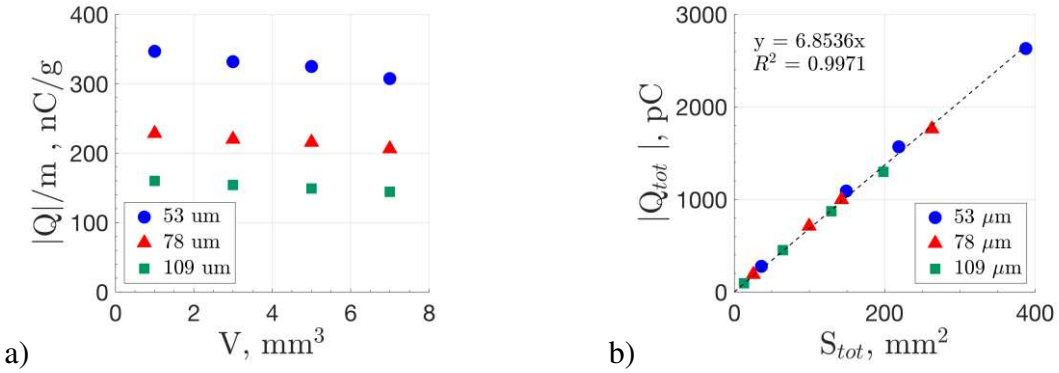

Figure 9. Charge level (in absolute value) acquired after 20 ms by glass ballotini reported as: a) charge-to-mass ratio vs sample volume, b) total charge vs total surface area

A comparison of the simulation results with some of the experimental data reported by Zafar et al. [9] for glass ballotini is shown in Figure 10. The particle size is slightly different between the two works, as they used a narrow sieve cut, whilst mono size spheres were used in the simulations. Other conditions, i.e. the dispersion pressure pulse (0.5 barg) and sample volume (3 mm^3) are kept the same. A decreasing trend of the specific charge with particle size is found in both experiments and simulations, as expected. An excellent agreement is found for the finest particles, for which the charge-to-mass ratio differs only by less than 10%. The larger is the particle size, the higher is the discrepancy between experimental and simulation results, with the latter overestimating the value.

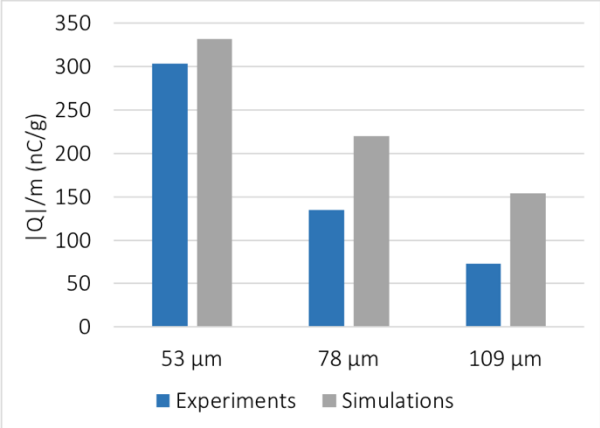

Figure 10. Comparison of the specific charge of the glass ballotini obtained by DEM-CFD simulations with the experimental results of Zafar et al. [9] (3 mm^3 sample volume, 0.5 barg dispersion pressure)

The particle charge distribution at the end of the dispersion process is shown in Figure 11 for a simulation with 1 mm^3 of 78 µm glass particles. The ~~red~~ data points represent the final charge on each particle at the end of the simulation divided by the equilibrium charge value. Most of the charges accumulated on the particles are higher than 60% of the equilibrium charge. The data are reported as a function of the product between the number of impacts and the average impact velocity for each particle, as this particular way of plotting them shows a rather clear trend. Interestingly, the exponential macroscopic dependence can be represented by: $y = 1 - e^{-x/C}$. The parameter determined by a fitting procedure is C = 77 m/s with a determination coefficient R^2 = 0.97. The same fitting equation is found to apply for all the simulations with glass ballotini. However, the data dispersion increases with increasing number of particles, as shown by the determination coefficients reported in Table 5 for different sample volumes.

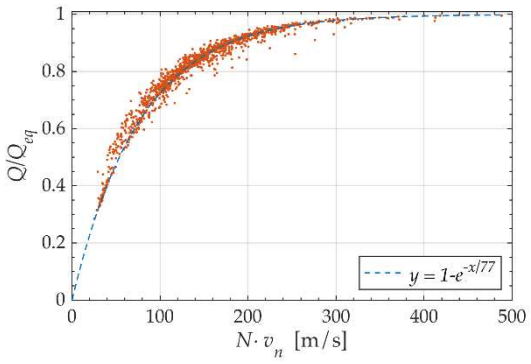

Figure 11 Final charge on each particle of the simulation normalized with the equilibrium charge value. The data are reported as a function of the product between number of impacts and average impact velocity for each particle. An exponential trend is also shown. 78 µm particles glass ballotini, 1 mm^3 sample.

Table 5 Characteristics of the macroscopic exponential model for simulations with glass ballotini.

Sample volume (mm^3)	Diameter (μm)	C (m/s)	R^2
1	53	78	0.94
	78	77	0.97
	109	77	0.97
7	53	81	0.64
	78	79	0.74
	109	78	0.80

Figure 12 shows the probability density function of the surface charge density, σ, at the end of the simulation for glass ballotini samples having different diameters. The results show that the distribution width is roughly similar for the three cases considered, even for the 109 μm sample that has only 343 particles. Moreover, the most frequent values of charge are larger than the mean of the distribution and close to the equilibrium charge value, represented by the rightmost bar of the histogram in all the three cases considered.

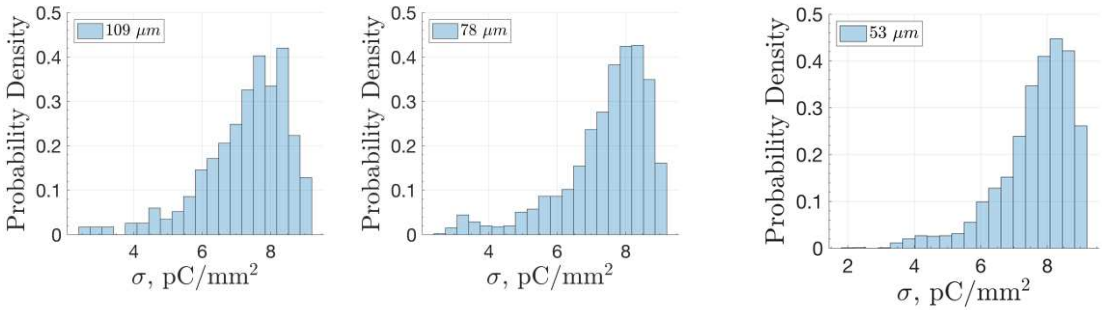

Figure 12 Charge distribution at the end of the simulation for three sizes of glass ballotini (bulk sample volume of $1mm^3$)

4.5 Particle-particle charge transfer

For monodisperse particles made of the same material (i.e. having the same apparent work function) appreciable charge is transferred only between particles with different charge levels, as shown by Choudhury et al. [52, 53]. So, interparticle charge exchange is not expected to be notable. Indeed, to highlight the importance of this effect, simulations have been carried out whilst deactivating triboelectric charging due to particle-particle collisions. The percentage of variation in the final total charge between simulations with and without particle-particle contact charging is very small in all the cases considered (4 sample volumes, 3 particle diameters). The

error increases with the sample volume, but even for the largest volume it does not exceed 0.8%. Moreover, this value relates to 53 μm particles and for the larger sizes it is much smaller. The results confirm that the role of interparticle collisions is essentially to redistribute the charges acquired during particle wall collisions. This may not be the general case if particles made of different materials are present in the sample or even if there is significant size polydispersity [5, 16].

4.6 Triboelectric charging of pharmaceutical powders

The simulation results for α-LM and aspirin particles (109 μm) are shown in Figure 13 for 1 mm^3 samples as a cumulative graph of the total charge on the particles as a function of time, with the results of glass ballotini added for comparison. As expected from the work function, particles of both materials charge negatively against stainless steel. Interestingly, all the particles leave the dispersion unit sooner than the pulse duration of 20 ms used in the experiments by Zafar et al. [9]. The shape of the lines is very similar for all the considered materials. The pharmaceutical particles charge significantly compared to glass ballotini because their apparent work function is higher than the one of glass (see Table 1), so a larger contact potential difference is observed when contacting stainless steel. Aspirin and α-LM particles also get charged to a higher percentage of the equilibrium charge value at the end of the simulation compared to glass ballotini, probably because they have a lower density compared to glass ballotini (hence accelerating faster to larger velocities), and are more compliant, so the contact area during impact is larger.

As shown in Table 6, the number of impacts does not change significantly for the three materials, while the maximum impact velocity is slightly larger for α-LM and aspirin, as they have smaller densities. Since the maximum contact area depends on the impact velocity and stiffness, the impact deformation contributes to the higher percentage of the equilibrium charge reached by α-LM and aspirin compared to glass. The charge-to-mass ratios for aspirin and α-LM samples are around 1350 and 900 nC/g, respectively, and do not change notably with sample volume.

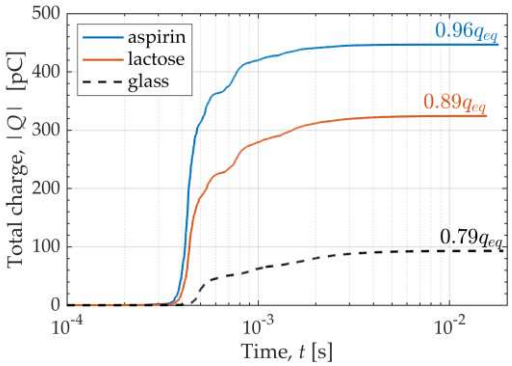

Figure 13. Total cumulative charge acquired by 1 mm^3 samples of α-LM, aspirin and glass ballotini (109 µm) as a function of time (log scale). The curves stop when all particles have left the system.

Table 6 Average number of particle-wall impacts and maximum normal particle-wall impact velocity for 109 µm particles for air pressure pulse of 0.5 barg

	N° of p-w impacts (average)			Max p-w impact velocity (m/s)		
Sample Volume	**glass**	**α-LM**	**aspirin**	**glass**	**α-LM**	**aspirin**
1 mm^3	15	15	16	51	62	64
3 mm^3	17	17	18	51	64	63
5 mm^3	17	16	17	53	53	55
7 mm^3	16	15	16	44	50	49

The simulation results show that the absolute value of the total charge varies linearly with the total surface area of the sample, similar to the trend for glass ballotini (see Figure 9b), yielding charge to surface area ratios of 34 and 24 pC/mm^2 for aspirin and α-LM, respectively. Watanabe et al. [39] report equilibrium charge values for large single particles of aspirin and α-LM (of about 550 µm diameter, obtained by near-mesh sieving), as -40 pC and -18 pC, respectively. Similar charge values were also found by Zafar et al. [9]. Using a rough estimate of the surface area of a single particles, calculated as the volume of a sphere having a 550 µm diameter, the equilibrium values of the surface charge density of aspirin and α-LM particles can be estimated from the recorded equilibrium charge values reported by Watanabe et al [39]. For aspirin, a value of 42 pC/mm^2 is obtained, while for α-LM it is about 19 pC/mm^2. The predicted surface charge densities from the simulations (i.e. 34 pC/mm^2 for aspirin and 24 pC/mm^2 for α-LM) are reasonably close.

Eilbeck et al. [54] analysed triboelectric charging of α-LM particles as they flow out of a cyclone into a catchpot. For 100 µm particles and with a gas velocity of 10 m/s, a charge-to-

mass ratio of about 100 nC/g was measured, which is lower than the value found in the present work (900 nC/g). The difference could be due to significantly lower particle velocities in the cyclone. The dispersion method used here tends to charge particles to the levels approaching their equilibrium charge value. Figure 14 shows the cumulative charge distribution on α-LM and aspirin particles for two sample volumes. The cumulative distributions are of sigmoidal shape and markedly shifted towards the equilibrium charge (reported with dashed lines). This effect is particularly evident for 1 mm^3 sample of aspirin, for which nearly 33% of particles exceed 99% of the equilibrium charge.

In summary, the above results show that the aerodynamic dispersion device analysed here has a good potential to be used as a characterization device for assessing the triboelectric charging tendency of powders. It charges the particles to near their equilibrium charge level, using a small sample quantity. This is particularly attractive in cases where the test material is scarce, such as new APIs still under development, for which a large quantity is usually unavailable.

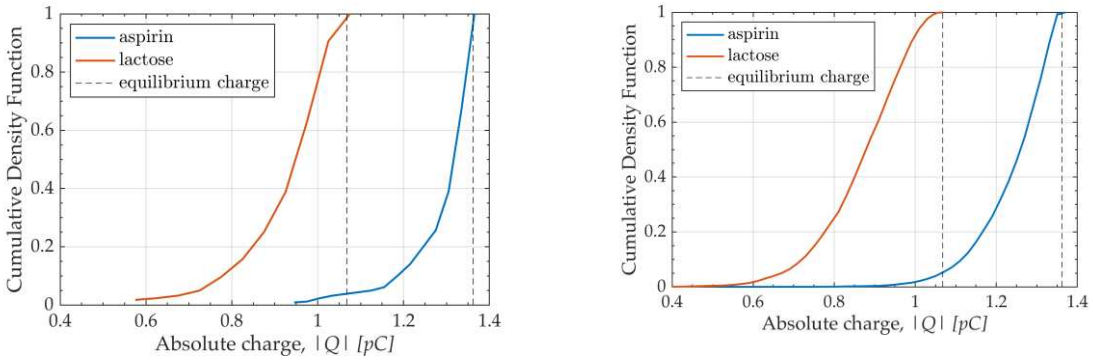

a) b)

Figure 14 Cumulative charge distribution at the end of the simulation for α-LM and aspirin particles. a) 1 mm^3 sample; b) 7 mm^3 sample.

5. Conclusions

DEM-CFD simulations of the triboelectrification of particles by aerodynamic dispersion have been carried out to investigate the dispersion and charging processes of a model particle system (glass ballotini) and two pharmaceutical powders (aspirin and α-LM). The simulated dispersion

555 device is based on the design of the powder dispersion unit of Morphology® G3 instrument of
556 Malvern Panalytical, Ltd. Four-way coupling is used to obtain the detailed solution of the air
557 flow and particle motion, including the effects of particle-particle and particle-wall collisions.
558 Careful evaluation of the critical model parameters was carried out to ensure realistic contact
559 and triboelectric model properties.

560 The air flow inside the unit gives rise to instantaneous air velocities above 200 m/s for an
561 applied air pressure pulse of 0.5 barg, exerting an intense transient drag on the particles. Particle
562 collision statistics for simulated glass ballotini shows that the particle-wall collisions could
563 reach to speeds up to 60 m/s for the small sample volume (1 mm^3) of the small particles analysed
564 (78 μm). Dispersing the same sample volume with larger particles (109 μm) leads to a lower
565 maximum impact speed of 51 m/s. The average p-w collision speeds for the two 78 μm sample
566 sizes of 1 mm^3 and 7 mm^3 are 5.6 m/s and 4.7 m/s, respectively, while lower average values are
567 recorded for particle-particle impacts (around 1.5 m/s). Dispersing larger particles (109 μm)
568 leads to similar average collision speeds.

569 The simulations outcome confirms the well-established experimental observations that the
570 tribocharging process produces the highest charge-to-mass ratio for the smallest particles up to
571 350 nC/g for 53 μm glass ballotini. Increasing the particle size causes a significant decrease in
572 the specific charge, confirming the dependence of the charging process on the specific solids
573 surface area. Indeed, a unique value for the net accumulated charge per unit surface area is
574 obtained, ~7 pC/mm^2, for all particle sizes of glass ballotini. Interparticle collisions do not
575 influence the final charge level by more than 1% of the total charge.

576 Aspirin and α-LM particles show a similar charging trend, but to different asymptotic
577 (equilibrium) levels. In these cases the number of particle impacts is similar to those of glass
578 ballotini, but the impact speeds are larger. The samples aspirin and α-LM get charged to almost
579 the maximum level, especially for small sample volumes. The surface charge density for aspirin
580 is calculated as 34 pC/mm^2, i.e. about eight times higher than that of glass ballotini, while the
581 value calculated for α-LM is 24 pC/mm^2. These charge levels corresponds to 96% and 89% of
582 the equilibrium surface charge densities of aspirin and α-LM, respectively. The corresponding
583 value for glass ballotini is lower at 79%, as they are denser and stiffer, deforming to a much
584 lesser extent on collisions.

585 The charge distributions on aspirin and α-LM particles at the end of the simulations are strongly
586 shifted towards their equilibrium charge values and the results are comparable with values of
587 equilibrium charge measured experimentally, suggesting that the considered dispersion device

588 is potentially useful for characterizing the triboelectric charging tendency of powders with
589 scarce availability, such as new APIs under development.

590

591 **ACKNOWLEDGEMENTS**
592
593 The experimental data used in this work have been extracted from the previous work carried
594 out at the University of Leeds by the first author on the Erasmus Exchange Programme and
595 cited accordingly.
596

References

[1] S. Matsusaka, H. Maruyama, T. Matsuyama, M. Ghadiri, Triboelectric charging of powders: A review, Chem. Eng. Sci. 65 (2010) 5781–5807. https://doi.org/10.1016/j.ces.2010.07.005.

[2] S. Naik, R. Mukherjee, B. Chauduri, Triboelectrification: A review of experimental and mechanistic modeling approaches with a special focus on pharmaceutical powders, International journal of pharmaceutics, 510 (2016) 375-385. https://doi.org/10.1016/j.ijpharm.2016.06.031

[3] J. Yao, J. Li, Y. Zhao, C.-H. Wang, Characterization of granular electrostatics generation, Powder Technol. 363 (2020) 74–85. https://doi.org/10.1016/J.POWTEC.2020.01.028.

[4] R. Cocco, A. Issangya, S.B.R. Karri, T. Freeman, H.M. Jaeger, T.M. Knowlton, Small-scale particle interactions are having significant effects on global fluidized bed behavior, KONA Powder Part. J. 34 (2017) 155–167. https://doi.org/10.14356/kona.2017021.

[5] S.R. Waitukaitis, V. Lee, J.M. Pierson, S.L. Forman, H.M. Jaeger, Size-dependent same-material tribocharging in insulating grains, Physical Review Letters, 112 (2014), 218001. https://doi.org/10.1103/PhysRevLett.112.218001

[6] T. Matsuyama, H. Yamamoto, Charge-relaxation process dominates contact charging of a particle in atmospheric condition: II. The general model, Journal of Physics D: Applied Physics, 30 (1997), 2170. https://doi.org/10.1088/0022-3727/30/15/008

[7] D.J. Lacks, T. Shinbrot, Long standing and unresolved issues in triboelectric charging, Nature Reviews Chemistry 3 (2019), 465-476. https://doi.org/10.1038/s41570-019-0115-1

[8] A. Zarrebini, M. Ghadiri, M. Dyson, P. Kippax, F. McNeil-Watson, Tribo-electrification of powders due to dispersion, Powder Technol. 250 (2013) 75–83. https://doi.org/10.1016/j.powtec.2013.10.006.

[9] U. Zafar, F. Alfano, M. Ghadiri, Evaluation of a new dispersion technique for assessing triboelectric charging of powders, Int. J. Pharm. 543 (2018) 151–159. https://doi.org/10.1016/j.ijpharm.2018.03.049.

[10] S. Saifoori, W. P. Goh, M. Ali, M. Ghadiri, Impact breakage of acicular crystals. Powder Technology, 361 (2020), 651-662. https://doi.org/10.1016/j.powtec.2019.11.061

[11] W.P. Goh, M. Ali, K. Sinha, N.K. Nere, R. Ho, S. Bordawekar, A. Sheikh, M. Ghadiri, Assessment of impact breakage of carbamazepine dihydrate due to aerodynamic dispersion, Int. J. Pharm. 572 (2019) 118780. https://doi.org/10.1016/J.IJPHARM.2019.118780.

[12] J. Wong, P.C.L. Kwok, & H.K. Chan, Electrostatics in pharmaceutical solids. Chemical Engineering Science, 125 (2015), 225-237. https://doi.org/10.1016/j.ces.2014.05.037

[13] M. Ali, M. Ghadiri, Analysis of triboelectric charging of particles due to aerodynamic dispersion by a pulse of pressurised air jet, Adv. Powder Technol. 28 (2017) 2735–2740. https://doi.org/10.1016/j.apt.2017.07.026.

[14] S. Matsusaka, M. Ghadiri, H. Masuda, Electrification of an elastic sphere by repeated impacts on a metal plate, , Journal of Physics D: Applied Physics, 33 (1995), 2311. https://doi.org/10.1088/0022-3727/33/18/316

[15] Ray, M., Chowdhury, F., Sowinski, A., Mehrani, P., & Passalacqua, A. (2019). An Euler-Euler model for mono-dispersed gas-particle flows incorporating electrostatic charging due to particle-wall and particle-particle collisions. Chemical Engineering Science, 197, 327-344.

[16] Ray, M., Chowdhury, F., Sowinski, A., Mehrani, P., & Passalacqua, A. (2020). Eulerian modeling of charge transport in bi-disperse particulate flows due to triboelectrification. Physics of Fluids, 32(2), 023302.

[17] S. Golshan, R. Sotudeh-Gharebagh, R. Zarghami, N. Mostoufi, B. Blais, J.A.M. Kuipers, Review and implementation of CFD-DEM applied to chemical process systems, Chem. Eng. Sci. 221 (2020) 115646. https://doi.org/10.1016/J.CES.2020.115646.

[18] M.W. Korevaar, J.T. Padding, M.A. Van der Hoef, J.A.M. Kuipers, Integrated DEM-CFD modeling of the contact charging of pneumatically conveyed powders, Powder Technol. 258 (2014) 144–156. https://doi.org/10.1016/j.powtec.2014.03.020.

[19] M.A. Hassani, R. Zarghami, H.R. Norouzi, N. Mostoufi, Numerical investigation of effect of electrostatic forces on the hydrodynamics of gas-solid fluidized beds, Powder Technol. 246 (2013) 16–25. https://doi.org/10.1016/j.powtec.2013.05.007.

[20] J. Kolehmainen, A. Ozel, C.M. Boyce, S. Sundaresan, A hybrid approach to computing electrostatic forces in fluidized beds of charged particles, AIChE J. 62 (2016) 2282–2295. https://doi.org/10.1002/aic.15279.

[21] E.W.C. Lim, Mixing behaviors of granular materials in gas fluidized beds with electrostatic effects, Ind. Eng. Chem. Res. 52 (2013) 15863–15873. https://doi.org/10.1021/ie402511p.

[22] L. Konopka, J. Kosek, Discrete element modeling of electrostatic charging of polyethylene powder particles, J. Electrostat. 87 (2017) 150–157. https://doi.org/10.1016/j.elstat.2017.04.008.

[23] S. Naik, S. Sarkar, V. Gupta, B.C. Hancock, Y. Abramov, W. Yu, B. Chaudhuri, A combined experimental and numerical approach to explore tribocharging of pharmaceutical excipients in a hopper chute assembly, Int. J. Pharm. 491 (2015) 58–68. https://doi.org/10.1016/j.ijpharm.2015.05.081.

[24] R. Garg, T. Li, S. Pannala, Documentation of open-source MFIX–DEM software for gas-solids flows, 2012. https://mfix.netl.doe.gov/download/mfix/mfix_current_documentation/dem_doc_2012-1.pdf.

[25] T. Li, W.A. Rogers, M. Syamlal, J.-F. Dietiker, J. Musser, M. Shahnam, S. Rabha, The NETL MFiX Suite of multiphase flow models: A brief review and recent applications of MFiX-TFM to fossil energy Technologies, Chem. Eng. Sci. 169 (2017) 259–272. https://doi.org/10.1016/j.ces.2016.07.043.

[26] J.-F. Dietiker, T. Li, R. Garg, M. Shahnam, Cartesian grid simulations of gas–solids flow systems with complex geometry, Powder Technol. 235 (2013) 696–705. https://doi.org/10.1016/j.powtec.2012.11.028.

[27] F.P. Di Maio, A. Di Renzo, Analytical solution for the problem of frictional-elastic

collisions of spherical particles using the linear model, Chem. Eng. Sci. 59 (2004) 3461–3475. https://doi.org/10.1016/j.ces.2004.05.014.

[28] M. Syamlal, W. Rogers, T.J. O`Brien, MFIX documentation theory guide, United States, 1993. https://doi.org/10.2172/10145548.

[29] S. Zimmermann, F. Taghipour, CFD Modeling of the Hydrodynamics and Reaction Kinetics of FCC Fluidized-Bed Reactors, Ind. Eng. Chem. Res. 44 (2005) 9818–9827. https://doi.org/10.1021/IE050490+.

[30] H. Grosshans, M. V. Papalexandris, A model for the non-uniform contact charging of particles, Powder Technol. 305 (2017) 518–527. https://doi.org/10.1016/J.POWTEC.2016.10.024.

[31] S. Matsusaka, H. Masuda, Electrostatics of particles, *Advanced Powder Technology 14* (2003), 143-166. https://doi.org/10.1163/156855203763593958

[32] C. Pei, C.-Y. Wu, D. England, S. Byard, H. Berchtold, M. Adams, Numerical analysis of contact electrification using DEM-CFD, Powder Technol. 248 (2013) 34–43. https://doi.org/10.1016/j.powtec.2013.04.014.

[33] C. Pei, C.-Y. Wu, D. England, S. Byard, H. Berchtold, M. Adams, DEM-CFD modeling of particle systems with long-range electrostatic interactions, AIChE J. 61 (2015) 1792–1803. https://doi.org/10.1002/aic.14768.

[34] C. Pei, C.-Y. Wu, M. Adams, DEM-CFD analysis of contact electrification and electrostatic interactions during fluidization, Powder Technol. 304 (2016) 208–217. https://doi.org/10.1016/j.powtec.2016.08.030.

[35] Matsuyama, T., & Yamamoto, H. (1995). Characterizing the electrostatic charging of polymer particles by impact charging experiments. Advanced Powder Technology, 6(3), 211-220.

[36] R. P. Feynman, R. B. Leighton, M. Sands (1963). The Feynman lectures in physics, mainly electromagnetism and matter, vol. *II Redwood City: Addison Wesley*.

[37] Di Renzo, A., & Di Maio, F. P. (2004). Comparison of contact-force models for the simulation of collisions in DEM-based granular flow codes. Chemical engineering science, 59(3), 525-541.

[38] K.L. Johnson, Contact mechanics, Cambridge University Press, 1987.

[39] H. Watanabe, M. Ghadiri, T. Matsuyama, Y.L. Ding, K.G. Pitt, H. Maruyama, S. Matsusaka, H. Masuda, Triboelectrification of pharmaceutical powders by particle impact, Int. J. Pharm. 334 (2007) 149–155. https://doi.org/10.1016/j.ijpharm.2006.11.005.

[40] S. Naik, S. Sarkar, B. Hancock, M. Rowland, Y. Abramov, W. Yu, B. Chaudhuri, An experimental and numerical modeling study of tribocharging in pharmaceutical granular mixtures, Powder Technol. 297 (2016) 211–219. https://doi.org/10.1016/J.POWTEC.2016.04.013.

[41] S. Trigwell, N. Grable, C.U. Yurteri, R. Sharma, M.K. Mazumder, Effects of surface properties on the tribocharging characteristics of polymer powder as applied to industrial processes, IEEE Trans. Ind. Appl. 39 (2003) 79–86. https://doi.org/10.1109/TIA.2002.807228.

[42] C.F. Gallo, W.L. Lama, Some charge exchange phenomena explained by a classical

model of the work function, J. Electrostat. 2 (1976) 145–150. https://doi.org/10.1016/0304-3886(76)90005-X.

[43] J.J.P. Stewart, Optimization of parameters for semiempirical methods II. Applications, J. Comput. Chem. 10 (1989) 221–264. https://doi.org/10.1002/jcc.540100209.

[44] J.J.P. Stewart, MOPAC2016, (n.d.). http://openmopac.net/manual/index.html.

[45] Fullmer, W. D., & Musser, J. (2018). CFD-DEM solution verification: Fixed-bed studies. Powder technology, 339, 760-764.

[46] Volk, A., Ghia, U., & Liu, G. R. (2018). Assessment of CFD-DEM solution error against computational cell size for flows through a fixed-bed of binary-sized particles. *Powder Technology*, *325*, 519-529.

[47] A. Zarrebini, Tribo-electric charging of powders due to dispersion, University of Leeds, 2012.

[48] W. R. Harper (1967). *Contact and frictional electrification*. Clarendon P..

[49] K. Saleh, A. Aghili, The spatio-temporal evolution of tribo-electric charging transfer during the pneumatic conveying of powders: modelling and experimental validation. Chem. Eng. Sci. 68 (2011) 120-131.

[50] M. Murtomaa, E. Rasanen, J. Rantanen, A. Bailey, E. Laine, J. Mannermaa, J. Yliruusi, Electrostatic measurement on a miniaturized fluidized bed, J. Electrost. 57 (2002).

[51] A.G. Bailey, C.J.A. Smedley, The impact charging of polymer particles, Adv. Powder Technol. (1991) 277-284

[52] Chowdhury, F., Sowinski, A., Ray, M., Passalacqua, A., & Mehrani, P. (2018). Charge generation and saturation on polymer particles due to single and repeated particle-metal contacts. Journal of Electrostatics, 91, 9-15.

[53] Chowdhury, F., Elchamaa, B., Ray, M., Sowinski, A., Passalacqua, A., & Mehrani, P. (2020). Apparatus design for measuring electrostatic charge transfer due to particle-particle collisions. Powder Technology, 361, 860-866.

[54] J. Eilbeck, G. Rowley, P. A. Carter, E. J. Fletcher, Effect of contamination of pharmaceutical equipment on powder triboelectrification, International journal of pharmaceutics 195 (2000) 7-11.